The Astrophysical Journal, 848:121 (15pp), 2017 October 20 https://doi.org/10.3847/1538-4357/aa8e9f

A Measurement of the Cosmic Microwave Background *B*-mode Polarization Power Spectrum at Subdegree Scales from Two Years of POLARBEAR Data

The POLARBEAR Collaboration,
P. A. R. Ade[1], M. Aguilar[2], Y. Akiba[3,4], K. Arnold[5], C. Baccigalupi[6,7], D. Barron[8], D. Beck[9], F. Bianchini[10], D. Boettger[11], J. Borrill[8,12], S. Chapman[13], Y. Chinone[14,15], K. Crowley[5], A. Cukierman[14], R. Dünner[11], M. Dobbs[16], A. Ducout[15], T. Elleflot[5], J. Errard[9], G. Fabbian[17], S. M. Feeney[18,19], C. Feng[20], T. Fujino[21], N. Galitzki[5], A. Gilbert[16], N. Goeckner-Wald[14], J. C. Groh[14], G. Hall[22], N. Halverson[23,24,25], T. Hamada[4,26], M. Hasegawa[3,4], M. Hazumi[4,3,15,27], C. A. Hill[14,28], L. Howe[5], Y. Inoue[4,29], G. Jaehnig[23,24], A. H. Jaffe[19], O. Jeong[14], D. Kaneko[15], N. Katayama[15], B. Keating[5], R. Keskitalo[8,12], T. Kisner[8,12], N. Krachmalnicoff[6], A. Kusaka[28,30], M. Le Jeune[9], A. T. Lee[14,28,31], E. M. Leitch[32,33], D. Leon[5], E. Linder[8,28], L. Lowry[5], F. Matsuda[5], T. Matsumura[15], Y. Minami[4], J. Montgomery[16], M. Navaroli[5], H. Nishino[4], H. Paar[5], J. Peloton[34], A. T. P. Pham[10], D. Poletti[6,7], G. Puglisi[6,7], C. L. Reichardt[10], P. L. Richards[14], C. Ross[13], Y. Segawa[3,4], B. D. Sherwin[28], M. Silva-Feaver[5], P. Siritanasak[5], N. Stebor[5], R. Stompor[9], A. Suzuki[14,31], O. Tajima[3,4], S. Takakura[4,35], S. Takatori[3,4], D. Tanabe[3,4], G. P. Teply[5], T. Tomaru[4], C. Tucker[1], N. Whitehorn[14], and A. Zahn[5]
[1] School of Physics and Astronomy, Cardiff University, Cardiff CF10 3XQ, UK
[2] Departamento de Física, FCFM, Universidad de Chile, Blanco Encalada 2008, Santiago, Chile
[3] SOKENDAI (The Graduate University for Advanced Studies), Hayama, Miura District, Kanagawa 240-0115, Japan
[4] High Energy Accelerator Research Organization (KEK), Tsukuba, Ibaraki 305-0801, Japan
[5] Department of Physics, University of California, San Diego, CA 92093-0424, USA
[6] The International School for Advanced Studies, SISSA, Via Bonomea 265, I-34136, Trieste, Italy
[7] The National Institute for Nuclear Physics, INFN, Sezione di Trieste Via Valerio 2, I-34127, Trieste, Italy
[8] Space Sciences Laboratory, University of California, Berkeley, CA 94720, USA
[9] AstroParticule et Cosmologie, Université Paris Diderot, CNRS/IN2P3, CEA/Irfu, Obs de Paris, Sorbonne Paris Cité, France
[10] School of Physics, University of Melbourne, Parkville, VIC 3010, Australia
[11] Centro de Astro-Ingeniería, Pontificia Universidad Católica de Chile, Vicuña Mackenna 4860, Santiago, Chile
[12] Computational Cosmology Center, Lawrence Berkeley National Laboratory, Berkeley, CA 94720, USA
[13] Department of Physics and Atmospheric Science, Dalhousie University, Halifax, NS, B3H4R2, Canada
[14] Department of Physics, University of California, Berkeley, CA 94720, USA; chinoney@berkeley.edu
[15] Kavli IPMU (WPI), UTIAS, The University of Tokyo, Kashiwa, Chiba 277-8583, Japan
[16] Physics Department, McGill University, Montreal, QC H3A 0G4, Canada
[17] Institut d'Astrophysique Spatiale, CNRS (UMR 8617), Université Paris-Sud, Université Paris-Saclay, bât. 121, F-91405 Orsay, France
[18] Center for Computational Astrophysics, Flatiron Institute, 162 5th Avenue, New York, NY 10010, USA
[19] Department of Physics, Blackett Laboratory, Imperial College London, London SW7 2AZ, UK
[20] Department of Physics and Astronomy, University of California, Irvine, CA 92697-4575, USA
[21] Yokohama National University, Yokohama, Kanagawa 240-8501, Japan
[22] Harvard-Smithsonian Center for Astrophysics, Harvard University, Cambridge, MA 02138, USA
[23] Center for Astrophysics and Space Astronomy, University of Colorado, Boulder, CO 80309, USA
[24] Department of Physics, University of Colorado, Boulder, CO 80309, USA
[25] Department of Astrophysical and Planetary Sciences, University of Colorado, Boulder, CO 80309, USA
[26] Astronomical Institute, Graduate School of Science, Tohoku University, Sendai, 980-8578, Japan
[27] Institute of Space and Astronautical Science (ISAS), Japan Aerospace Exploration Agency (JAXA), Sagamihara, Kanagawa 252-0222, Japan
[28] Physics Division, Lawrence Berkeley National Laboratory, Berkeley, CA 94720, USA
[29] Institute of Physics, Academia Sinica, 128, Sec.2, Academia Road, Nankang, Taiwan
[30] Department of Physics, University of Tokyo, Tokyo 113-0033, Japan
[31] Radio Astronomy Laboratory, University of California, Berkeley, CA 94720, USA
[32] Department of Astronomy and Astrophysics, University of Chicago, Chicago, IL 60637, USA
[33] Kavli Institute for Cosmological Physics, University of Chicago, Chicago, IL 60637, USA
[34] Department of Physics & Astronomy, University of Sussex, Brighton BN1 9QH, UK; j.peloton@sussex.ac.uk
[35] Department of Earth and Space Science, Osaka University, Toyonaka, Osaka 560-0043, Japan
Received 2017 May 5; revised 2017 September 7; accepted 2017 September 20; published 2017 October 23

Abstract

We report an improved measurement of the cosmic microwave background *B*-mode polarization power spectrum with the POLARBEAR experiment at 150 GHz. By adding new data collected during the second season of observations (2013–2014) to re-analyzed data from the first season (2012–2013), we have reduced twofold the band-power uncertainties. The band powers are reported over angular multipoles $500 \leqslant \ell \leqslant 2100$, where the dominant *B*-mode signal is expected to be due to the gravitational lensing of *E*-modes. We reject the null hypothesis of no *B*-mode polarization at a confidence of 3.1σ including both statistical and systematic uncertainties. We test the consistency of the measured *B*-modes with the Λ Cold Dark Matter (ΛCDM) framework by fitting for a single lensing amplitude parameter A_L relative to the *Planck* 2015 best-fit model prediction. We obtain $A_L = 0.60^{+0.26}_{-0.24}(\mathrm{stat})^{+0.00}_{-0.04}(\mathrm{inst}) \pm 0.14(\mathrm{foreground}) \pm 0.04(\mathrm{multi})$, where $A_L = 1$ is the fiducial ΛCDM value.

Key words: cosmic background radiation – cosmology: observations – large-scale structure of universe

1. Introduction

The polarization of the cosmic microwave background (CMB) encodes broad cosmological information that is the focus of current and future generations of CMB experiments. The pattern of linear polarization separates into gradient-like *E*-mode and curl-like *B*-mode components. On one hand, *E*-mode polarization is generated by the same scalar density fluctuations which generate temperature anisotropies in the ionized plasma before recombination. In contrast, *B*-mode polarization is not generated by these scalar perturbations and could be generated by either tensor perturbations (gravitational waves) from inflation or conversion of *E*-modes to *B*-modes by gravitational lensing along the line of sight. On degree scales, where the inflation scenario predicts *B*-mode polarization of the CMB from primordial gravitational waves, no such signal has yet been detected (The BICEP2/Keck and Planck Collaborations et al. 2015; Planck Collaboration et al. 2016d; The BICEP2 and Keck Array Collaborations et al. 2016). In addition, gravitational lensing, which is not related to this primordial signal, induces a characteristic peak in the BB angular power spectrum at $\ell \sim 1000$. In this case, the primary *E*-mode spectrum is converted to *B*-modes by lensing from the large-scale distribution of matter. Several experiments have begun to measure this lensing *B*-mode signal, including POLARBEAR (The POLARBEAR Collaboration et al. 2014a), BICEP2 (The BICEP2 Collaboration et al. 2014), Keck Array (The BICEP2 and Keck Array Collaborations et al. 2015), SPTPOL (Keisler et al. 2015), cross-spectra between BICEP2/Keck Array and *Planck* 2015 *B*-mode maps (The BICEP2/Keck and Planck Collaborations et al. 2015; The BICEP2 and Keck Array Collaborations et al. 2016), and ACTPOL (Louis et al. 2017).

This paper reports results from the POLARBEAR telescope, which has a $3.'5$ resolution, giving its best sensitivity through intermediate angular scales around the $\ell \sim 1000$ lensing peak. A previous POLARBEAR publication (The POLARBEAR Collaboration et al. 2014a, hereafter PB14) reported the first direct measurement of a non-zero *B*-mode signal, with modest significance. In this paper, we present an improved measurement of the angular power spectrum as measured by POLARBEAR in the same survey areas (a few degrees across for each sky patch), to greater depth. The procedure used to analyze the data set shares many similarities with that described in PB14. In particular, the analysis is conducted blindly, with angular power spectra revealed only when the data pass a series of null tests and systematic-error checks. We also incorporate many new features and improvements in the analysis as well as an improved discussion of the contribution of astrophysical foregrounds. We include not only new data taken between 2013 October and 2014 April (hereafter called the second season) but also a reprocessing of the first-season data (2012 May–2013 June); together these changes expand the total data volume with respect to PB14 by a factor of 61%. This means 62% of the total data are reprocessed and 38% of the total data are newly processed. We therefore refer the reader to the descriptions in PB14 when necessary, emphasizing here only the additional steps.

In Section 2, we describe the two seasons of data collected by the POLARBEAR instrument. In Section 3, we discuss the calibration procedure, and the data analysis steps are outlined in Sections 4–6. In Section 7, we show the power spectra results, and in Section 8, we draw our conclusions.

2. First and Second Season Observations of the POLARBEAR Instrument

POLARBEAR is a CMB experiment that has been observing from the 2.5 m Huan Tran Telescope since 2012 January. The telescope is located at the James Ax Observatory at an elevation of 5190 m in the Atacama Desert in Chile. The POLARBEAR receiver consists of an array of 1274 transition-edge sensor bolometers cooled to 0.3 K and observing the sky through lenslet-coupled double-slot dipole antennas. Within the array, the bolometers are grouped into seven different wafers. More details on the receiver and telescope can be found in Arnold et al. (2012) and Kermish et al. (2012). A cold half-wave plate (HWP) is positioned on the sky side of the cryogenic lenses in the receiver. Although this HWP was stepped almost daily for the first half of the first season, it was not stepped during the rest of the first season or during the second season. We discuss the role of the HWP on the mitigation of instrumental systematic effects in Section 4.4.

The POLARBEAR observing strategy is described in PB14 and is summarized here. We observe three CMB fields, with each one visible for 6–8 hr per day. The three patches are centered at (R.A., decl.) = ($4^{\rm h}40^{\rm m}12^{\rm s}$, -45° $00'$), ($11^{\rm h}53^{\rm m}0^{\rm s}$, -0° $30'$), and ($23^{\rm h}1^{\rm m}48^{\rm s}$, -32° $48'$), which we call RA4.5, RA12, and RA23, respectively. We divide the observations into constant elevation scans (CESs) during which the telescope scans back and forth in azimuth at constant elevation. We call each sweep in azimuth a subscan. After approximately 15 minutes, when the patch has moved out of the field of view, we adjust the elevation and begin another CES.

The total observation time for the two seasons and the three CMB patches is 4700 hr, corresponding to 33% of the total calendar time available for the two seasons. Of this time, 2800 hr pass all of the data quality checks described in Section 4.2 and are used to compute the power spectrum. As mentioned, this is an increase in data volume of 61% over PB14.

The process of extracting cosmological results from raw time-ordered data (TOD) can be summarized in three steps: calibration of the raw data, map making, and power-spectrum estimation. In the following two sections, we describe these processes.

3. Calibration

Before creating maps of the CMB polarization anisotropy, we characterize detector and telescope performance. This includes reconstructing the telescope pointing, measuring the beam, calibrating the detector TOD, and determining the detectors' polarization properties. We will describe each of these four steps in the following sections.

3.1. Pointing

To go from TOD to maps, we need to know where each detector was pointing as a function of time. We determine the pointing model using observations of bright extended and point-like millimeter sources selected from known source catalogs (Wrobel et al. 1998; Murphy et al. 2010) across a wide range in azimuth and elevation. The approach is similar to that of PB14, although the model had to be extended to handle the increased pointing data volume and sky coverage. Relative

to PB14, we use three times more pointing data across a ∼19% (∼30%) larger range in azimuth (elevation). Five new parameters were added to the pointing model to enable the pointing to be reconstructed over a larger fraction of the sky. The first was a timing error, i.e., an offset in hour angle per period of time, caused by small synchronization errors between clocks and ephemerides. The next two, solar radiation flexure in azimuth and elevation, account for the small deformation of the telescope due to temperature gradients related to the Sun's position. The final two, ambient temperature flexure in azimuth and elevation, are similar except with the deformation correlated with the ambient temperature (Matsuda 2017) Neglecting the four new flexure terms would worsen the rms pointing uncertainty by 8″.

The final pointing accuracy is similar to PB14, with an rms scatter measured on known radio source positions of 27″ and 30″ for seasons 1 and 2, respectively.

3.2. Beam

We estimate the beam map and its effective window function, B_ℓ, using dedicated observations of Jupiter, following the procedure outlined in PB14. However, for this analysis, we conservatively discarded the observations of Jupiter taken when the atmospheric precipitable water vapor (PWV) exceeded a threshold of 4 mm (as was also done for CMB observations), despite no clear sign of detector saturation in the reported range of angular scales. As a consistency check, we estimated the B_ℓ for each observation season separately to test potential variation over time and found no significant deviation. Consistent results were derived using Saturn observations. We tested that the deconvolution of the bolometer time constants induced a negligible change in the beam properties and window function. The main lobes of the beam are well-approximated by a Gaussian core having $3\farcm5 \pm 0\farcm1$ FWHM plus a diffraction tail asymptotically decaying as $1/\theta^3$, where θ is the radial coordinate of the beam profile (Hasselfield et al. 2013). The $1/\theta^3$ decay is a natural consequence of the presence of a Lyot stop in the optical chain as well as the finite detector size and difference in the spectral response of the detectors. In Figure 1, we show the mean radial profile of the beam obtained as an inverse noise weighted average of the beam profiles estimated for each single Jupiter observation in our data set together with the best-fit results of the beam profile model. The difference between the B_ℓ band powers derived from the best-fit profile model (orange curve) and the reference one derived from the Jupiter maps (red curve) is less than 1.5% in all of the ℓ ranges considered in this work.

The median beam ellipticity measured across the array is 5%, and the median difference in ellipticity measured for two channels in each focal plane pixel is 1.6%, with a subdegree difference in the ellipticity orientation. In the systematics simulations of Section 4.4, we use the full distributions of those two quantities to quantify the potential biases due to beam effects on the B-mode power spectrum.

The Jupiter-measured beam is then symmetrized radially and convolved with a pointing error term for each of the three fields to calculate the per-field beam as a function of angular multipole that will be used in the power spectrum analysis. The profile of the symmetrized beam is consistent with the radial profile data as shown in Figure 1. We refer the reader to PB14 for more details on the process.

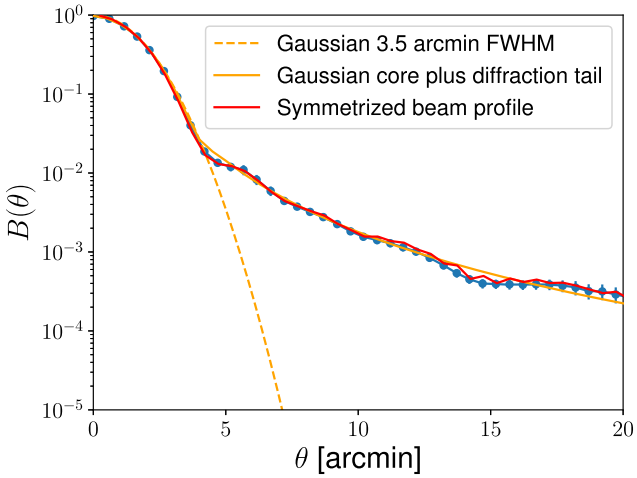

Figure 1. Mean POLARBEAR beam profile (blue points) as a function of the radial distance θ. The mean profile has been computed as an inverse noise weighted average of all of the beam profile measurements in our data set. The error bars show the 2σ error on the weighted mean. The results for the fit of the data to a Gaussian profile and to a model including a Gaussian core and a $1/\theta^3$ diffraction tail are shown by the dashed and solid lines, respectively. The radial profile of the beam estimated from the Jupiter maps is shown in red.

The pointing error calculation has changed slightly from PB14, although the underlying model is unchanged. We assume that the real instrumental pointing is Gaussian-distributed around the reconstructed pointing with a standard deviation referred to as the pointing jitter. In PB14, the pointing jitter and uncertainty on the jitter were calculated by fitting a beam width to subsets of the data to obtain a probability density function for the real jitter. However, further analysis showed that the underlying CMB anisotropies at each source's location are a significant bias in the fitted beam width, an effect not captured in the previous analysis. As in PB14, each point source is fitted using free parameters for source position, amplitude, and beam width. The uncertainty on the parameters is then estimated from the scatter of the fitted parameters for point sources simulated using the central fitted values against a ΛCDM CMB temperature background. The pointing jitter and its uncertainty are then backed out of the fitted parameters and their uncertainties obtained from simulations. Using this algorithm, we find pointing jitter values of $24\farcs5 \pm 2\farcs7$, $24\farcs5 \pm 5\farcs9$, and $57\farcs1 \pm 6\farcs1$ for RA4.5, RA12, and RA23, respectively. These jitter values are consistent with those found in the PB14 analysis, but with significantly reduced error bars due to the correct treatment of the underlying CMB fluctuations.

3.3. Detector Gains

We calibrate the TOD to physical Rayleigh–Jeans Kelvin temperature units (K_{RJ}) in a multistep process, following the methods of PB14. First, we determine the relative calibration between detectors over time using a combination of an internal thermal source and Saturn observations. With this relative calibration in hand, we can turn the TOD into a temperature map. Finally, we determine the absolute calibration by looking at the temperature anisotropy CMB power spectrum as discussed in Section 6. In this section, we will focus on the relative calibration process.

Table 1
Uncertainties in Polarization Angle

Angle Uncertainty (°)	Global	Wafer Averaged
Beam uncertainties	0.11	0.33
Relative gain uncertainties	0.11	0.28
Non-ideality of HWP	0.18	0.19
Circular polarization of Tau A	0.10	0.05
HWP angle uncertainties	0.31	0.04
Pixel pointing uncertainties	<0.01	0.05
Bolometer time constant	0.01	0.04
Filtering effect	0.02	0.04
Total uncertainty (°)	0.40	0.48

Note. Systematic uncertainties in the global reference and wafer-averaged polarization angle, as measured using Tau A.

In brief, the relative calibration of the TOD proceeds in three steps. The first step combines an internal thermal calibration source (the stimulator) with the flux from Saturn. We discuss the complications introduced by Saturn's rings in the Appendix. Next, we correct for the effect due to the polarized emission from the stimulator, which is then rotated by the HWP. We thus define the HWP angle-dependent template by considering observations of a variety of astrophysical sources at different HWP rotation angles. In addition to the HWP position, the polarized response also depends on the status of the stimulator (a few hardware changes were made over the observing period) and potentially a long-term temporal drift. As a consequence, we generate a new polarization template for each of six epochs (four for season 1 and two for season 2) corresponding to changes in the stimulator hardware. Finally, we combine the stimulator and Saturn observations to calculate the relative gain, which is the conversion from electrical current into K_{RJ} units, for each detector and observation.

The median variation of the relative gain calibration for all detectors between two consecutive stimulator measurements is 0.5%; we use this information for the systematic-error estimate to quantify the impact of the drift of the gains on the *B*-mode power spectrum (see Section 4.4).

3.4. Polarization Angle

As in PB14, we determine the relative detector polarization angles using daily observations of Tau A (the Crab Nebula). We then further improve the accuracy in the global polarization angle by nulling the C_ℓ^{EB} cross-spectrum (see Section 6), assumed to be zero. Here, we summarize this approach, with more details available in PB14. We also tabulate the achieved polarization angle uncertainties from this analysis, which are important to the systematics budget for the C_ℓ^{BB} power spectrum (see Section 4.4).

We estimate polarization angles and efficiencies by observing Tau A daily for roughly 30 minutes and fitting each detector's TOD from the two seasons of data to a reference Tau A map from the IRAM[36] 30 m telescope observation (Aumont et al. 2010) using the POLARBEAR Jupiter-based beam and known pointing information. The individual-pixel angular uncertainty in each wafer is estimated to be 1°.2 using the measured angular dispersions in each wafer. In addition, the total systematic uncertainties for the array-averaged and wafer-averaged angles are 0°.40 and 0°.48, respectively. A detailed breakdown can be found in Table 1. By combining the two seasons of data, the systematic uncertainties from the beam and the relative gain uncertainties causing temperature-to-polarization leakage are improved compared to PB14. However, the polarization angle difference between the seasons described below shows that the HWP angle uncertainty is now more significant than what was found in PB14. These changes make the total polarization angle uncertainty the same level as that of PB14.

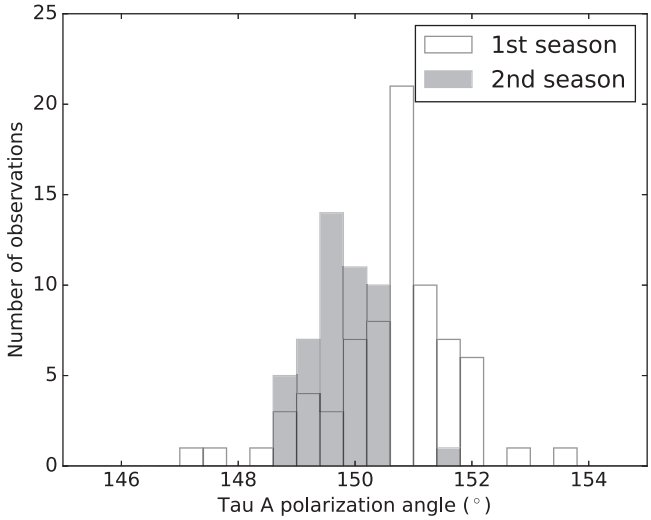

Figure 2. Tau A polarization angles from daily observations in the first season (unfilled) and the second season (shaded).

The array-averaged polarization efficiency was 97.2%, consistent with the expected value of 97.6% from HWP and anti-reflection coatings. The systematic uncertainty for the polarization efficiency is 1.6%, which introduces a 3.3% multiplicative uncertainty in the CMB *B*-mode power spectrum.

We also checked the stability of the array-averaged polarization angles over time. Figure 2 shows a histogram of the measured array-averaged Tau A polarization angles. Each angle is calculated by computing $(1/2)\arctan(\sum U_j/\sum Q_j)$ across map pixels within 10′ of the center of Tau A, where Q_j and U_j are the Stokes Q and U in the map pixel j. Two effects are apparent: (1) the average angle shifted by 0°.9 between the two seasons, and (2) the scatter was larger in season 1. We believe that both effects are due to the uncertainty of the HWP position. The polarization angle calculation is based on the commanded HWP positions (quantized at 11°.25). Any offset, $\Theta_{\rm err}$, between the commanded and actual HWP position will shift the calculated polarization angle by $2\Theta_{\rm err}$. The first-season data were taken at a number of HWP positions (where multiple HWP offsets lead to the increased scatter in the polarization angle), while the second-season data were taken at a single HWP position (where the single HWP offset shows up as a polarization angle offset between the first and second seasons). We can reconstruct the distribution of HWP offsets that would lead to the observed polarization angle variations and find the typical magnitude to be 0°.28 (a polarization angle uncertainty of 0°.56). After unblinding the C_ℓ^{EB} spectrum, we found that season-by-season C_ℓ^{EB} nulling led to a consistent shift in the polarization angle. The two-season combined Tau A polarization angle was $150°.4 \pm 0°.2(\mathrm{stat}) \pm 0°.8(\mathrm{sys})$ in equatorial

[36] Institut de Radioastronomie Millimétrique.

coordinates using the C_ℓ^{EB}-derived polarization angle described in Section 6.

4. Data Analysis

As mentioned, the two-season data set contains about 61% more data than the PB14 data set. This increase corresponds to new data from the second season of observation, as well as a reanalysis of the data from the first season with the improvements made in calibration and data selection, as detailed in the other sections. The main update to the data analysis with respect to PB14 has been the implementation of a second and complementary pipeline to analyze the data set for more robust results through consistency checks and improved systematic-error control. Although the calibration of the TOD (see Section 3) is shared between the two pipelines, they perform map-making and the power-spectrum estimation differently.

4.1. Map Making and Power-spectra Estimation

We adopt two independent and algorithmically different pipelines in the analysis: the first pipeline (hereafter "pipeline A") is based on the MASTER method (Hivon et al. 2002) and was described in PB14, and the second pipeline (hereafter "pipeline B") is based on the work described in Poletti et al. (2016). The main steps performed by the two pipelines to estimate sky maps, angular cross-spectra, and null cross-spectra are described in Figure 3.

The pipeline-A and pipeline-B map-making algorithms differ slightly in their filtering of the calibrated data and substantially in the way they project the filtered TOD onto maps. Both perform high-pass and azimuthal filters to remove atmospheric noise and ground pickup, respectively. Pipeline A performs these two operations sequentially while pipeline B performs them simultaneously.[37] In addition, pipeline A applies a low-pass filter prior to map making. The pipeline-A map-making algorithm projects the time-domain data into maps without accounting for the filtering-induced power suppression, but accounts for this during the power-spectrum estimation. Combined with the sequential filtering, this allows a substantial speed-up compared to the other pipeline. Pipeline B accounts for the filtering of the TOD and produces unbiased maps. The two pipelines also use different pixelization schemes. Pipeline A projects the time-domain data onto flat sky maps using a cylindrical equal-area projection, with map pixels of width $2'$. Pipeline B projects the time-domain data onto curved-sky maps using the `HEALPix`[38] pixelization ($N_{\rm side} = 2048$, i.e., map pixel width $\sim 1.'7$; Górski et al. 2005). Given the relatively small fraction of sky observed (a few degrees across for each patch) and the resolution of the telescope ($3.'5$), both approaches remain equivalent. In both pipelines, the data are combined into chunks, which are later cross-correlated to avoid noise biases in the estimated power spectra. After the data selection (see Section 4.2), pipeline A splits the two-season data sets into 214, 212, and 269 daily maps for RA4.5, RA12, and RA23, respectively; pipeline B splits the data sets into eight chunks of data for each patch corresponding to roughly 1.5 cumulative months of data each. The full-season temperature and

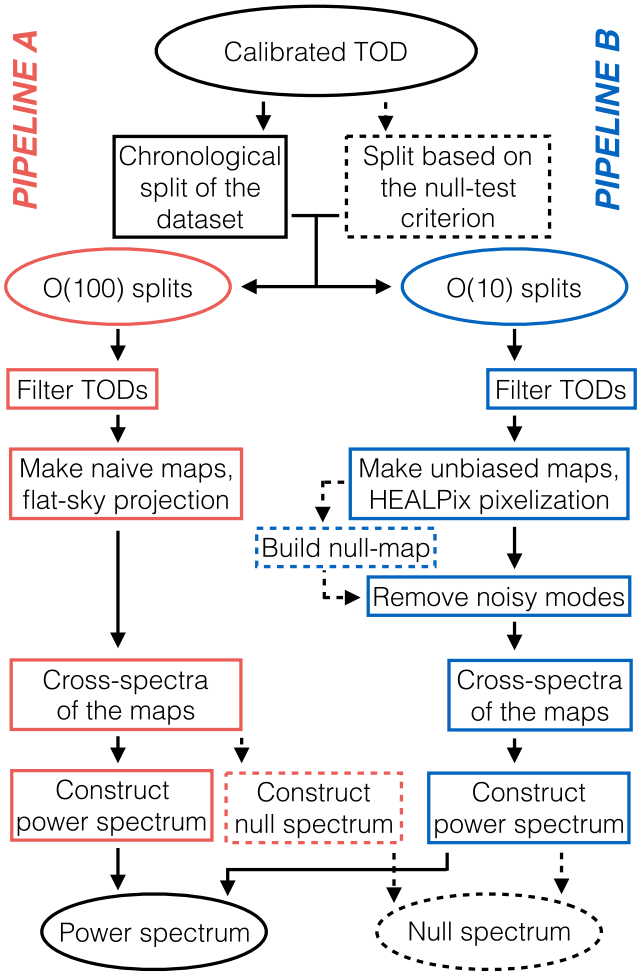

Figure 3. Schematic view of the main steps performed by pipelines A (red) and B (blue). The main steps starting from the calibrated TOD and leading to the production of angular cross-spectra are shown with solid boxes and arrows. In addition, extra steps related to the production of null cross-spectra used to assess the quality of the data set are shown with the dashed boxes and arrows. See the text for detailed information.

Stokes Q and U maps of RA23 produced by the two pipelines are plotted in Figure 4. The resulting polarization white-noise levels reach 7, 6, and 5 μK arcmin (10, 7, and 6 μK arcmin with the beam and filter transfer function divided out) for RA4.5, RA12, and RA23, respectively, for pipeline A.

In both pipelines, the power-spectrum estimators are based on the pure pseudo-C_ℓ technique (Smith 2006) although they differ in a few aspects, such as the computation of the mode–mode mixing matrix and the handling of the off-diagonal elements controlling the level of E-to-B leakage. For pipeline A, the formalism was described in PB14. For pipeline B, we use the software `X^2pure` (Grain et al. 2009, 2012; Ferté et al. 2013). As described in Poletti et al. (2016), we perform a map-domain removal of the noisiest modes in order to control large-scale noise. Figure 4 shows the effective maps after performing this mode removal. We estimate the statistical uncertainty on the C_ℓ^{EB} and C_ℓ^{BB} spectra from 500 signal and noise Monte Carlo simulations (100 for pipeline B) as described in Section 7. For pipeline A, thanks to a realistic uncertainty estimate as well as an overall larger data set and improved calibration, this release achieves almost twice the sensitivity of PB14. As a result of applying different treatments to the data, the estimated statistical uncertainties from the two

[37] This is desirable in general as the templates that need to be filtered out are not always orthogonal from the outset. However, this step makes the map-making process more complex than filtering the non-orthogonal templates one after another.

[38] http://healpix.jpl.nasa.gov/

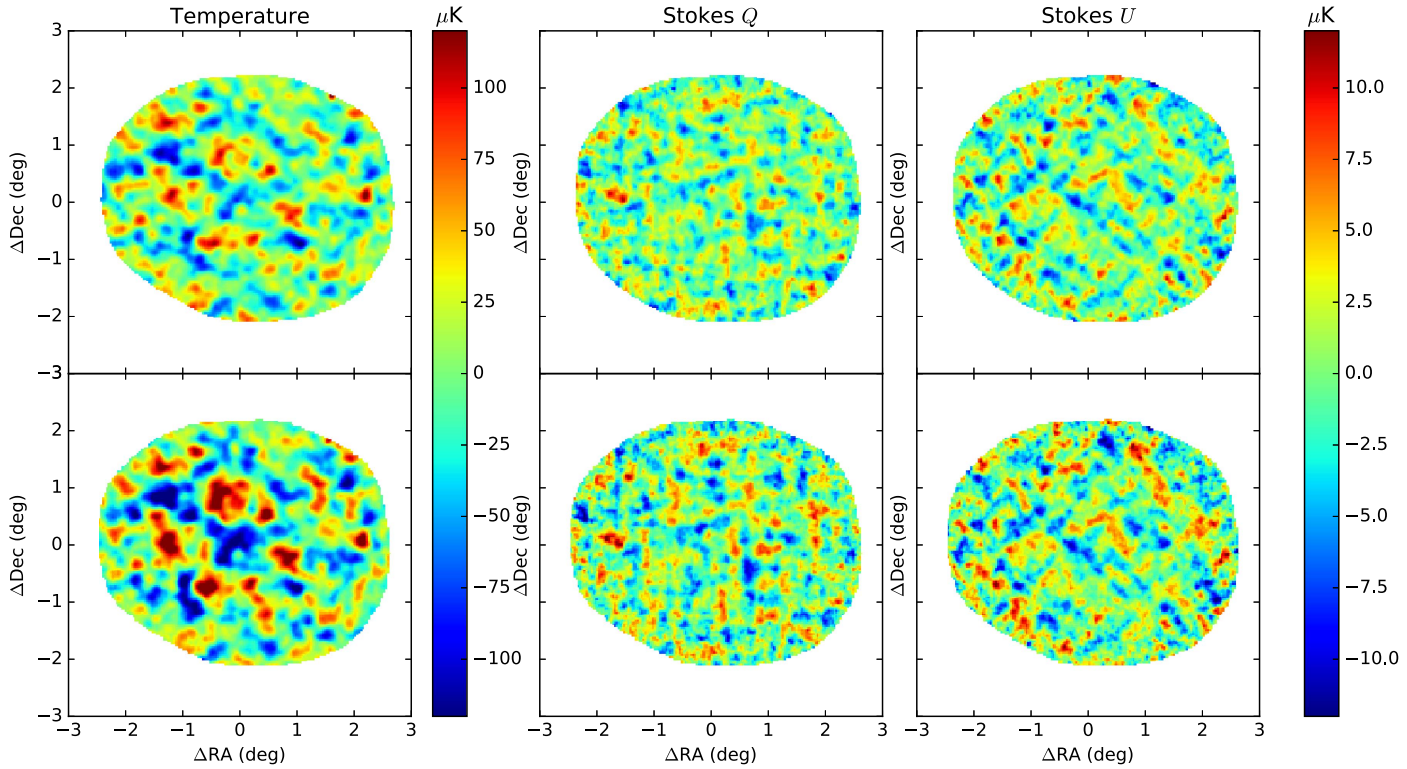

Figure 4. POLARBEAR CMB intensity and polarization sky maps of RA23 in equatorial coordinates. The left, center, and right panels show the temperature anisotropy, Stokes Q, and Stokes U, respectively. The top maps are generated by pipeline A, and the bottom maps are generated by pipeline B (resampled with a map-pixel width of $2'$ and reprojected onto a cylindrical equal-area projection to ease the comparison). In both sets of maps, the maps are smoothed with a Gaussian filter with $3'.5$ FWHM, and, for visualization only, we show an area in which the map weights are above -10 dB. The polarization angle is defined with respect to the north celestial pole. Although the structures are clearly in agreement between the two sets of maps, as expected, the amplitude of the signal is different due to the fact that the two pipelines treat the amplitudes of the modes in the maps differently (Section 4.1 for details). Maps with alternative color schemes are available at http://bolo.berkeley.edu/polarbear/data/polarbear_BB_2017/.

pipelines are different (see Poletti et al. 2016 for a complete comparison of methods), being on average 20% higher for pipeline B. Part of this difference is also attributed to the difference of the resulting sky area used in the two analyses.

In PB14, POLARBEAR implemented a blind analysis method in our measurement of the B-mode polarization, and we adopted the same procedure for the two-season analysis. In the following, we describe the data selection, analysis validation by a null-test framework, instrumental systematic-error estimation, and foreground estimation including biases from contamination due to point-like extra-Galactic and polarized Galactic foregrounds.

4.2. Data Selection

In this section, we describe the data quality cuts. As mentioned in Section 2, 60% of the total CMB observation data (2800 hr out of 4700 hr) end up being included in the science analysis of this work. We do not select the other 40% due to some combination of bad weather, incomplete observations, or hardware glitches. Note that the thresholds for the latter were validated and finalized while running the suite of null tests described in the next section and before unblinding.

The data quality checks proceed in three stages. First, we require a successful measurement of the detector gains for each CES (see Section 3.3 for details on how detector gains are estimated). Second, we discard data based on conditions such as the level of PWV in the atmosphere, the angle between the observed patch and the Sun or the Moon, as well as measures of the quality of the data, such as the bolometer yield being too low, problematic scan length, bad azimuth encoder data, or the array median gain changing too rapidly, for example. This step can remove data from an entire CES or some of the detector channels within a CES, leaving ∼10,000 and ∼4000 CES for season 1 and season 2, respectively. Note that thanks to the improved calibration and slightly different data selection, the definition of season 1 here is not strictly equivalent to that used in PB14; the change increased by approximately 15% of the observation-hours that went into the maps. In the end, 2800 observation-hours pass both the first and second data quality checks. The volume of data from the second season is smaller than the one from the first season mainly because the period of observing time is smaller (13 months for the first season and 6 months for the second season). The third step goes further and consists of defining subscans (a constant-velocity segment of a timestream) and among them, identifying contaminated subscans (such as by finding glitches in them). As in PB14, we discard all data obtained while the telescope is accelerating.

4.3. Analysis Validation: Null Tests

We perform a suite of null tests to evaluate the calibration, data selection criteria, and filtering methods, and to test for unknown systematic errors before unblinding the data. This task consists of iteratively running the null-test framework

described in PB14, with the addition of three new data splits, until a set of predefined criteria (described below) is passed. Due to the non-negligible extra computational cost of pipeline B with respect to pipeline A,[39] the full set of null tests (see Section 4.3.1) is performed only by pipeline A as detailed in PB14. We primarily used these null tests by pipeline A to define the data selection criteria. Once the science data set is defined, pipeline B performs a subset of the data splits probed by pipeline A. The way pipeline B computes null spectra differs slightly from pipeline A. It first splits the data set in two according to the null-test criterion; second, it computes unbiased maps of four (or eight) disjoint subsets of each split; null maps are then computed by taking the difference of maps that belong to different splits; and finally, it computes and co-adds the cross-spectra of the null maps to form a null spectrum. Nevertheless, pipeline B performs further checks allowed by the production of null maps in addition to null spectra. These include the visual inspection of the null maps and the study of the individual cross-spectra of null maps and their distribution (the same data can contribute to several cross-spectra). More specifically, if the band powers of a null spectrum have a probability-to-exceed (PTE; see also Section 4.3.2) less than 5%, we study the cross-spectra of which it is the average, and we make sure that the low PTE is not determined by the cross-spectra involving the same particular portion of the data set. None of those extra checks found signs of contamination or inconsistencies in the data set. We emphasize that this large variety of validation tests is made possible by combining the complementary strengths of the two pipelines.

4.3.1. Data Splits

Null tests are performed for several interesting splits of the data, chosen to be sensitive to various sources of systematic contamination or miscalibration. In addition to the null tests we performed in PB14 ("first half versus second half of the data set," "rising versus setting," "high elevation versus low elevation," "high gain versus low gain," "good versus bad weather," "pixel type,"[40] "left versus right side of the focal plane," "left- versus right-going subscan," and "Moon distance"), we introduced the following three new tests to check the difference between seasons and our possible concerns:

1. "First season versus second season": probing seasonal variation on year-long timescales. This test is sensitive to systematic changes in the calibration, beams, telescope, and detectors.
2. "Sun distance": checking for residual contamination after setting the Sun-proximity threshold for an observation to be considered for analysis.
3. "Sun above the horizon versus Sun below the horizon": checking for contamination from the far sidelobe of the beam and systematic changes of the pointing due to the small deformation of the telescope by solar heating.

The 12 null tests are used to analyze the data set, and the correlations between the tests are taken into account in the analysis by also running the same suite of null tests on Monte Carlo (MC) simulations as described below. For the three sky patches, pipeline A then runs a total of 36 null tests, while pipeline B focuses on a subset of 11 null tests.

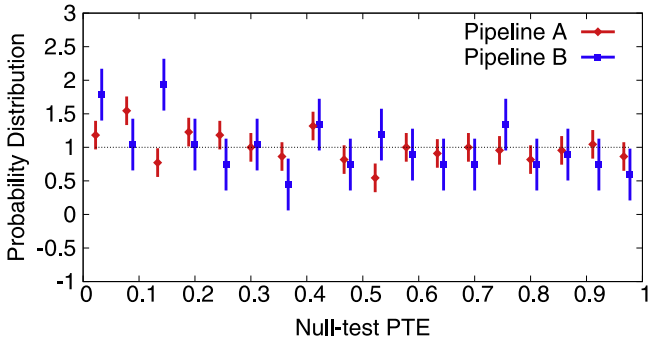

Figure 5. Null-test-PTE distribution for $\chi^2_{\rm null}$ for both pipeline A (red, 396 entries) and pipeline B (blue, 121 entries). Both distributions are consistent with the expected uniform distribution.

4.3.2. Analysis

In the null spectra, for each band-power bin b, we calculate the statistic $\chi_{\rm null}(b) \equiv \hat{C}_b^{\rm null}/\sigma_b$, where σ_b is an MC-based estimate of the corresponding standard deviation, and its square $\chi^2_{\rm null}(b)$. $\chi_{\rm null}(b)$ is sensitive to systematic biases in the null spectra, while $\chi^2_{\rm null}(b)$ is more sensitive to outlier bins. To probe for systematic contamination affecting a particular power spectrum or null-test data split, we calculate the sum of $\chi^2_{\rm null}(b)$ over $500 < b < 2100$ by spectrum ("$\chi^2_{\rm null}$ by spectrum") and the sum for both spectra for a specific test ("$\chi^2_{\rm null}$ by test"). We consider both C_ℓ^{EB} and C_ℓ^{BB} in the null tests in order to investigate sources of spurious B-mode signals. We require each of these sets of PTEs to be consistent with a uniform distribution, as evaluated using a Kolmogorov–Smirnov test, requiring a p-value (probability of seeing deviation from uniformity greater than that which is observed given the hypothesis of uniformity) to be equal to or greater than 5%. These distributions are consistent with the uniform distribution and Figure 5 shows the PTE distribution of the $\chi^2_{\rm null}$ for the two pipelines.

We create test statistics based on these quantities to search for different manifestations of systematic contamination. The five test statistics are PTEs from (1) the average value of $\chi_{\rm null}$; the extreme value of $\chi^2_{\rm null}$ (2) by bin, (3) by spectrum, and (4) by test; and (5) the total $\chi^2_{\rm null}$ summed over the 12 null tests. In each case, the result from the data is compared to the result from the simulations, and the PTEs are calculated. Finally, we combine each of the test statistics, and calculate the final PTE, requiring it to be equal to or greater than 5%. Table 2 shows the PTE values for the final configuration.

Comparing the most significant outlier from the five test statistics with that from signal and noise simulations, pipeline A (pipeline B) obtains PTEs of 71.8% (77%), 65.2% (16%), and 16.6% (13%) for RA4.5, RA12, and RA23, respectively. We therefore achieve the requirements described above, finding no evidence for systematics or miscalibration in the POLARBEAR data set used for the analysis and in the analysis process itself.

[39] A single map-making run of pipeline B uses roughly as much computation time as one full run of the null-test framework of pipeline A.
[40] Each detector wafer has two different pixel polarization angles.

Table 2
PTEs Resulting from the Null Test Framework

Patch	Average of $\chi_{\rm null}(b)$		Extreme of $\chi_{\rm null}(b)$		Extreme of $\chi^2_{\rm null}$ by $C_\ell^{EB/BB}$		Extreme of $\chi^2_{\rm null}$ by Test		Total $\chi^2_{\rm null}$	
	Pipeline		Pipeline		Pipeline		Pipeline		Pipeline	
	A	B	A	B	A	B	A	B	A	B
RA4.5	84.0%	100%	70.8%	49%	86.0%	54%	64.0%	73%	35.4%	47%
RA12	70.8%	9%	29.8%	19%	66.2%	52%	57.8%	54%	51.0%	52%
RA23	95.0%	91%	40.8%	13%	69.4%	11%	42.8%	16%	5.0%	5%

Note. PTEs resulting from the null-test framework. No significantly low or high PTE values are found, consistent with a lack of systematic contamination or miscalibration in the POLARBEAR data set and analysis. The only exception is the average $\chi_{\rm null}(b)$ of RA4.5 for pipeline B. The 100% PTE results from all 100 noise-only simulations having worse $\chi_{\rm null}(b)$ than the data. The possibility that this is caused by overestimation of the error bars is, however, excluded: this would produce a distribution of the PTEs skewed high (in contrast with Figure 5). Note that the PTE values in each patch are not independent from one another.

4.4. Analysis Validation: Simulations of Instrumental Effects

We describe in this section the signal-only simulations used to determine the effect of uncertainties in the instrument model on the power spectrum listed in Table 5 (subsection "Instrument"). We investigate nine systematic instrumental effects: uncertainty in the instrument polarization angle; uncertainty in the relative pixel polarization angles; uncertainty in the instrument boresight pointing model; differential pointing between the two detectors in a pixel; the drift of the gains between two consecutive thermal source calibrator measurements; relative gain-calibration uncertainty between the two detectors in a pixel; crosstalk in the multiplexed readout; differential beam size; and differential beam ellipticity.

The pipeline used to analyze those systematic effects was described in PB14, while here we describe two improvements: (1) the systematics pipeline follows exactly all of the data analysis pipeline steps, and (2) all instrumental systematics studied are now included within the systematics pipeline. The first modification makes the systematic-error study more comprehensive than that in PB14, i.e., the simulations performed here also include time-domain filtering and the cross-correlation of submaps. The second modification allows us to have a common framework for all effects, and therefore the same metric to analyze the results (i.e., we now include beam effects and electrical crosstalk, which were analyzed separately in PB14). Although the procedure was developed for both data analysis pipelines, we report here only the results from pipeline A due to computing constraints.

A major change in the hardware configuration with respect to PB14 is the position of the HWP. As mentioned in Section 3.4, we recorded the data beginning from the middle of the first season without stepping the HWP in order to decrease the scatter in the polarization angle of the detector. We found that this results in less mitigation of some instrumental effects such as those related to instrument and pixel polarization angle, drift of the gains, or crosstalk in the multiplexed readout. We note, however, that pointing-related effects remain stable with respect to PB14, and we reduce the uncertainty coming from beam-related effects, thanks mainly to an improved characterization.

All nine effects and their combination were found to produce spurious *BB* power well below the statistical uncertainty in the measurement of C_ℓ^{BB}, as also shown in Figure 6. The individual effects are combined linearly to give the total contamination.

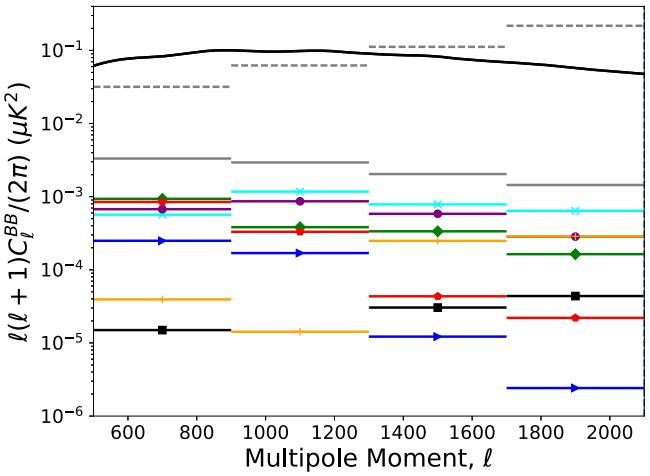

Figure 6. Estimated levels or upper bounds on instrumental systematic uncertainties in the four bins of the C_ℓ^{BB} power spectra, as described in Section 4.4. Individual effects (solid colors) and their combination (solid horizontal gray line) are displayed: combined uncertainty in instrument polarization angle and relative pixel polarization angles after self-calibration (purple circle), combined uncertainty in instrument boresight pointing model and differential pointing between the two detectors in a pixel (cyan cross), the drift of the gains between two consecutive thermal source calibrator measurements (red star), relative gain-calibration uncertainty between the two detectors in a pixel (green diamond), crosstalk in the multiplexed readout (blue arrow), differential beam shape (orange plus), and differential beam ellipticity (black square). For comparison, we display the binned statistical uncertainty from pipeline A (dashed horizontal line) reported in Table 4 and the theoretical *Planck* 2015 ΛCDM lensing *B*-mode spectrum (solid black line).

5. Foregrounds

Polarized Galactic and extra-Galactic foregrounds are a potential contaminant to the CMB and a particular concern for the very faint *B*-modes. As described in PB14, there are four foreground sources of interest: the first two are polarized Galactic dust and synchrotron emission, dominating at large angular scales (down to a few arcminutes) at intermediate and high Galactic latitudes; the second two are emission from polarized radio and dusty galaxies, on scales of a few arcminutes and smaller. In this section, we describe how we estimate the band-power contribution from each of these sources. Table 3 reports the mean values and 68.3% confidence intervals obtained for the band powers from the combination of the three patches for both components, and Figure 7 shows the

Table 3
Sources of Foreground Power and Their Expected Power in D_ℓ^{BB}

Foreground	Expected Power in D_ℓ^{BB} (10^{-4} μK^2)			
	$\ell = 500$–900	900–1300	1300–1700	1700–2100
Galactic dust	63.5 ± 123.3	53.6 ± 102.4	48.8 ± 91.4	46.9 ± 85.1
Galactic synchrotron	1.4 ± 2.1	1.2 ± 1.9	1.1 ± 1.7	1.0 ± 1.5
Radio & dusty galaxies	13.4 ± 5.5	26.8 ± 9.8	24.8 ± 15.3	67.4 ± 21.9
Total	78.3 ± 123.4	81.6 ± 102.9	74.7 ± 92.7	115.3 ± 87.9

Note. The total central value (uncertainty) on the final line is the linear (quadrature) sum of the individual foreground powers. Note that reported values for Galactic dust and synchrotron are upper limits and we have no detection of dust contamination nor of synchrotron contamination in our observed fields.

estimated foreground contributions to $\ell(\ell+1)C_\ell^{BB}/2\pi$ at a 68.3% confidence level. As can be seen, the total foreground contribution is estimated to be small in any band power, although not completely negligible.

Note that the methods employed to estimate the polarized Galactic dust and synchrotron contamination are different from those described in PB14, while the method used to estimate the contamination from radio and dusty galaxies remains similar. Indeed, in PB14, the estimates of the diffuse polarized foregrounds in the observed fields were based on models built upon the public data from *WMAP* and *Planck* at that time for the dust (Bennett et al. 2013; Planck Collaboration et al. 2014), as well as the QUIET levels reported for synchrotron (QUIET Collaboration et al. 2012). Between PB14 and this paper, the *Planck* 2015 polarization sky maps, including in particular the 353 GHz as the main tracer of the polarized Galactic dust emission, became available (Planck Collaboration et al. 2016a).[41] We therefore use these new data as the main reference for both the dust and synchrotron estimates reported below. It is relevant to notice also that, while carrying out the present analysis, we discovered a conversion error in the evaluation of the contamination from synchrotron emission in PB14, which, however, does not significantly change the conclusions there, and which has been reported in a separate erratum.

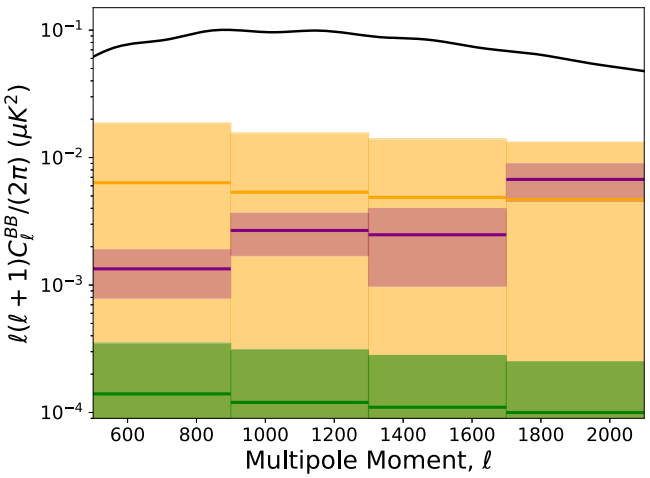

Figure 7. Estimated foreground contributions to $\ell(\ell+1)C_\ell^{BB}/2\pi$ at 68.3% confidence intervals in the multipole range $500 \leqslant \ell \leqslant 2100$: the upper limits on the polarized Galactic foregrounds, synchrotron (green shaded area) and thermal dust (orange shaded area), and the combined radio and dusty power (purple box). The solid horizontal lines represent the mean value in each band power (see Table 3). As can be seen, the foreground contributions are small, although not completely negligible. For comparison, a theoretical *Planck* 2015 ΛCDM spectrum (solid black line, see Section 6) is shown.

5.1. Polarized Galactic Dust and Synchrotron

The polarized Galactic foregrounds, synchrotron and thermal dust, dominate at frequencies smaller and larger than 70 GHz, respectively (Planck Collaboration et al. 2016b); at intermediate and high Galactic latitudes, and at the degree angular scale, the frequency of the foreground minimum seems to vary substantially, almost equally distributed between 60 and 90 GHz in regions where both foregrounds are detected with high significance (Krachmalnicoff et al. 2016). These Galactic foregrounds substantially contaminate CMB *B*-mode measurements at all frequencies on large angular scales, even in the cleanest regions of the sky, as shown in several recent studies (Krachmalnicoff et al. 2016; Planck Collaboration Int. XXX 2016). Nevertheless, Galactic foregrounds are expected to be subdominant with respect to the lensing *B*-modes at arcminute scales, and our purpose here is to assess their relevance and provide upper limits on their contribution to our observations.

For thermal dust, we adopt the following procedure. We take the publicly available *Planck* 2015 sky map at 353 GHz as a tracer of polarized emission from thermal dust. To avoid noise bias in the computation of spectra, we calculate cross-spectra using half-mission splittings using the `X2pure` power spectrum estimator. We evaluate statistical errors by means of white-noise MC simulations, using the pixel–pixel noise covariance matrices of the input maps. The low signal-to-noise ratio of the *Planck* 2015 polarization maps at high Galactic latitudes prevents the estimation of *B*-mode spectra directly in the regions corresponding to our patches because of their reduced size and the noise level at the small angular scales we consider. Therefore, in order to provide an upper limit on the amplitude of thermal dust, we compute power spectra on larger circular regions, with a 10° radius, centered on our sky patches. We extrapolate the measured amplitude of the spectra at $\ell \simeq 80$ (a multipole bin between 60 and 99) in these regions to higher multipoles by applying the power-law scaling $\mathcal{D}_l \propto \ell^{\alpha_d}$ with $\alpha_d = -0.42 \pm 0.02$ (Planck Collaboration Int. XXX 2016). We then scale the *Planck* 2015 measurements to the POLARBEAR frequency assuming a modified blackbody spectral dependence for the thermal dust, with temperature $T_d \simeq 19.6$ K and $\beta_d \simeq 1.59 \pm 0.14$ (Planck Collaboration Int. XXII 2015). To compute the extrapolation in frequency, we take into account both the *Planck* 2015 and the POLARBEAR frequency band passes, and for the extrapolation in ℓ, we consider the actual POLARBEAR band-power window function. To account for the

[41] https://www.cosmos.esa.int/web/planck/pla

fact that we are measuring the foreground amplitude on larger regions, we include in the error budget the Gaussian approximation of the signal sample variance evaluated for the actual sky area of the POLARBEAR patches.

A similar procedure has been used to estimate the amplitude of polarized synchrotron emission. We computed power spectra for synchrotron *B*-modes by cross-correlating the *Planck* 2015 Low Frequency Instrument 30 GHz map at the effective frequency of 28.4 GHz (Planck Collaboration et al. 2016a) with the *WMAP* *K* map at a frequency of 22.8 GHz (Bennett et al. 2013). Spectra are computed on the same circular regions of 10° radius. The measured amplitude at $\ell \simeq 80$ is rescaled in frequency considering a power-law frequency dependence with $\beta_s = -3.12 \pm 0.02$ (Fuskeland et al. 2014) and in multipole considering $\mathcal{D}_l \propto \ell^{\alpha_s}$ with $\alpha_s = -0.31 \pm 0.13$ (Planck Collaboration et al. 2016b).

We note that for both polarized Galactic dust and synchrotron, the limiting factor in our calculation of the foreground mean values and uncertainties comes from the *Planck* 2015 polarization noise level at such small angular scales. The level of contamination reported in this paper is therefore higher than in our previous PB14 estimates, which was based on models available at that time. In particular, the dominant contribution from Galactic dust, represented by the top of the orange area in Figure 7, increases by a factor of about 5 with respect to PB14.

5.2. Radio and Dusty Galaxies

We estimate the radio and dusty galaxy power by drawing 10,000 realizations from the distributions described below. In both cases, we take recent measurements of the temperature power and then convert it to polarization power using an estimate of the mean square polarization fraction. For radio galaxies, the temperature power estimate comes from the De Zotti et al. (2005) model at 150 GHz, which is scaled to the POLARBEAR effective frequency according to the measured spectral index for the radio sources of $\alpha_{\rm rg} = -0.90 \pm 0.20$ from George et al. (2015, hereafter G14). We ignore shot noise due to finite sky area, but assume a 10% calibration uncertainty on our nominal masking threshold of 25 mJy (i.e., the modeled threshold is 25 ± 2.5 mJy). We take the recent estimate from SPTPOL of the mean square polarization fraction for synchrotron sources of $\langle p^2 \rangle = (1.42 \pm 0.15) \times 10^{-3}$ (T. Crawford 2017, private communication).[42] These numbers are consistent with a recent analysis of brighter synchrotron sources in the 143 GHz *Planck* 2015 maps, which found $\sqrt{\langle p^2 \rangle} = 0.043 \pm 0.0018$, corresponding to $\langle p^2 \rangle = (1.85 \pm 0.15) \times 10^{-3}$ (Bonavera et al. 2017).

We use direct observations of the dusty galaxy power in temperature from G14. These include a Poisson term with $D^P_{3000} = 9.16 \pm 0.36\ \mu\mathrm{K}^2$ at the SPT frequency (150 GHz) and a spectral index of $\alpha_P = 3.267 \pm 0.077$, and a clustered term of the form $\ell^{0.8}$ normalized to $D^C_{3000} = 3.46 \pm 0.54\ \mu\mathrm{K}^2$ with a spectral index of $\alpha_C = 4.27 \pm 0.2$. Data on the polarization fraction of these dusty galaxies are still poor, but they are expected to have lower polarization fractions than the synchrotron sources. We conservatively draw the mean square polarization fraction $\langle p^2 \rangle$ from a uniform distribution between 1×10^{-4} and 1.57×10^{-3} (i.e., 1% polarized to the $+1\sigma$ limit from the G14 synchrotron measurement).

For each realization, we multiply the inferred dusty and radio galaxy spectra by the appropriate window functions to directly compare to the measured band powers.

6. Calibration using CMB Spectra

The absolute gain calibration is performed differently by the two pipelines. Pipeline A combines the estimate of C_ℓ^{TT} from each patch into one single estimate according to their statistical and beam uncertainties, and then estimates the absolute gain by fitting the patch-combined C_ℓ^{TT} to a theoretical *Planck* 2015 ΛCDM spectrum.[43] Finally, the correction is applied to the individual maps. Pipeline B estimates the absolute gain for each patch by first cross-correlating the POLARBEAR temperature maps with the foreground-cleaned *Planck* 2015 temperature map produced using the Spectral Matching Independent Component Analysis method (Planck Collaboration et al. 2016c). These cross-spectra are then compared to the corresponding POLARBEAR auto-spectra, before combining the estimates into a single absolute gain factor.

Both methods give consistent results; however, the second method gives a higher uncertainty due to the propagation of the noise in *Planck* 2015 data: 3.0% uncertainty on the absolute gain factor for pipeline A and 4.3% uncertainty for pipeline B. We note, however, that the method used by pipeline B has the advantage of being more cosmology independent. These calibration factors are then applied to all spectra by the respective pipelines to produce gain-calibrated spectra. The beam uncertainty is estimated from the uncertainty in the point-source-derived beam-smoothing correction (Section 3.2) and the variation in that correction across each field. We shift the simulated beam by 1σ, and find this beam shift leads to a ±1.0% change in the best-fit lensing *B*-mode amplitude. We include this 1.0% uncertainty as part of the multiplicative error budget. A complete breakdown of the multiplicative uncertainties can be found in Table 5.

The global instrument polarization angle correction $\Delta\psi$ is obtained by fitting the patch-combined C_ℓ^{EB} to $2\Delta\psi C_\ell^{EE}$ (Keating et al. 2013) for both pipelines. The best-fit value and statistical uncertainty in the global C_ℓ^{EB}-derived instrument polarization angle correction is $-0.^\circ79 \pm 0.^\circ16$ ($-0.^\circ67 \pm 0.^\circ17$) for pipeline A (pipeline B). Combining this value with the relative shift from the Tau A-derived angle (see Section 3.4), this result is consistent with the results obtained previously in PB14. Finally, pipeline A applies the polarization angle correction to the individual maps and pipeline B to the power spectra.

7. *B*-mode Power Spectrum Results

The final analysis procedure follows closely the final first-season analysis described in PB14. For each patch and each spectrum, we first form the covariance matrices using our set of 500 MC simulations (100 MC for pipeline B), and we then add the beam and gain-calibration uncertainties as described later in this section. We note that the use of MC simulations to construct the band-power covariance matrices gives more realistic estimates than the analytical expressions used in PB14. Finally, for both pipelines, a single estimate of the power spectra from the three patches is created using the measured band powers and their covariance matrices.

[42] https://cmb-s4.org/CMB-S4workshops/index.php/File:Sptpol_ptsrc_polfrac_500d.pdf

[43] All references to the *Planck* 2015 ΛCDM model in this work refer to the best-fit values for the `base_plikHM_TT_lowTEB_lensing` configuration.

Table 4
Reported POLARBEAR Band Powers $D_\ell^{BB} = \ell(\ell+1)C_\ell^{BB}/2\pi$ from Pipeline A

Central ℓ	D_ℓ^{BB} (μK^2)
700	$0.053^{+0.029}_{-0.026}$
1100	$0.074^{+0.057}_{-0.054}$
1500	$0.045^{+0.116}_{-0.109}$
1900	$0.352^{+0.260}_{-0.239}$

Note. The errors correspond to the 68.3% confidence intervals of the statistical uncertainty only. The multiplicative uncertainty (due, e.g., to the absolute calibration uncertainty) and systematic uncertainties are not included, but can be found in Table 5. Correlations between neighboring bins are small and consistent with zero within the statistical uncertainty of ± 0.05 due to the finite number of Monte Carlo simulation realizations.

The band-power covariance matrix accounts for the sample variance and instrumental noise variance. These contributions are estimated by means of 500 MC simulations that use the same pointing and detector weighting as the data, and take into account signal from a beam-convolved realization of a *Planck* 2015 ΛCDM power spectrum that includes the effect of gravitational lensing. As in PB14, we model the noise in the simulation as white, and we add random spectrally flat noise to the TOD of each detector variance equivalent to that measured from the detectors. For each detector, the noise variance is estimated from the average of the time-domain power spectral densities over 1–3 Hz, corresponding approximately to an ℓ range of 500–1500, and the filtering of the TOD is designed to suppress the correlated part of the noise in this frequency range. This choice of using white noise, as opposed to a model of correlated noise, has been validated with the null-test framework (Section 4.3).

Finally, we combine the per-patch power spectra into a single patch-combined spectrum according to the band-power covariance matrices. The diagonal elements of the patch-combined covariance matrix are used as the pipeline-B error bars shown in Figure 9. Note that the multiplicative uncertainty (due, e.g., to the absolute calibration uncertainty) and systematic uncertainties are not shown in Figure 9, but can be found in Table 5. For the released *B*-mode band powers from pipeline A, we go a step further and account for the slightly non-Gaussian shape of the band-power likelihoods using an offset log-normal distribution (Bond et al. 2000):

$$-2\ln\mathcal{L}(X_{\rm meas}|X_{\rm cosm}) = \frac{1}{\sigma^2}[\ln[X_{\rm meas}+x_0] - \ln[X_{\rm cosm}+x_0]]^2 - \ln[\sigma(X_{\rm meas}+x_0)\sqrt{2\pi}], \quad (1)$$

where $X_{\rm meas}$ is the measure of a parameter of interest X, and $X_{\rm cosm}$ is a fiducial value for this parameter (the *B*-mode band powers in this case). We fit for the values of σ and x_0 in each band using simulations with 0%, 69%, and 100% of the *B*-mode power predicted by the *Planck* 2015 ΛCDM model. The intermediate value of 69% was chosen as being close to the observed *B*-mode power. The values are reported in Table 4 along with the band powers. We use the same formalism to empirically model the likelihood for the *B*-mode amplitude parameters A_{BB} and A_L described below. We find that the average of the upper and lower error bars of the band powers (the *B*-mode amplitude) is a few percent smaller or larger (∼7% smaller) than that from using the Gaussian distribution. The shape of the likelihood is positively skewed, and the upper error bar is $\lesssim$10% (∼7%) larger than the lower error bar.

The combined C_ℓ^{TT}, C_ℓ^{EE}, C_ℓ^{TE}, C_ℓ^{TB}, and C_ℓ^{EB} spectra after the global calibration of the absolute gain and polarization angle are plotted in Figure 8. We find that the patch-combined and individual-patch spectra are consistent with the ΛCDM model. The patch-combined spectra from pipeline A (pipeline B) have a PTE with respect to the ΛCDM cosmology of 32% (28%), 62% (26%), 92% (67%), 79% (29%), and 60% (75%) for C_ℓ^{TT}, C_ℓ^{EE}, C_ℓ^{TE}, C_ℓ^{TB}, and C_ℓ^{EB}, respectively. The spectra from both pipelines are in good agreement.

The difference of the individual-patch C_ℓ^{BB} spectra from pipeline A and pipeline B has a PTE with respect to a null spectrum of 23%, where the variance of the null spectrum is derived from an analytical estimate. We remind the reader that the two pipelines treat noisy modes differently (see Poletti et al. 2016 for a detailed discussion), and we therefore expect a larger scatter between results in the noise-dominated regime ($\ell > 1300$).

The combined C_ℓ^{BB} spectra are shown in Figure 9, indicating that the spectra from both pipelines are in good agreement. The PTEs of these band powers with respect to the *Planck* 2015 ΛCDM spectrum are 55% (pipeline A) and 41% (pipeline B). Since the results using pipeline A have satisfied a larger set of the null tests and the instrumental systematic-error analysis was fully performed only on pipeline A, we adopt its power spectra results (tabulated in Table 4) as the reference (official) POLARBEAR results for this release. The results in Table 4 are the data that should be quoted or used for any further cosmological analysis.

First, we consider the significance with which these data rule out the null hypothesis of no *B*-modes. After setting the sample variance to zero, we fit for the amplitude parameter, finding $A_{BB} = 0.75^{+0.21}_{-0.20}({\rm stat})^{+0.00}_{-0.04}({\rm inst})$, where in this expression "stat" refers to the expected statistical fluctuation of the measurement ($X_{\rm meas}$ in Equation (1) with $X = A_{BB}$) evaluated with the likelihood of no lensing signal ($X_{\rm cosm} = 0$), and "inst" refers to the systematic uncertainty associated with possible biases from the instrument. To calculate the upper bound on the additive uncertainties from instrumental systematic errors, we linearly add, in each band, the upper bound of the band powers of all of the instrument systematic effects discussed in Section 4.4. This produces a lower A_{BB} and sets the lower bound of the additive uncertainty. To be conservative, we evaluate the detection significance by subtracting this systematic uncertainty of 0.04 from 0.75. The likelihood ratio is $\mathcal{L}(X_{\rm meas} = 0.71|X_{\rm cosm} = 0)/\max_{X_{\rm cosm}}\mathcal{L}(X_{\rm meas} = 0.71|X_{\rm cosm}) = 9.0\times10^{-3}$, corresponding to a 3.1σ rejection of the no *B*-mode null hypothesis.

Next, we fit the band powers to the *Planck* 2015 ΛCDM cosmological model with a single *B*-mode amplitude parameter, A_{BB}. We find $A_{BB} = 0.69^{+0.26}_{-0.25}({\rm stat})^{+0.00}_{-0.04}({\rm inst}) \pm 0.04({\rm multi})$, where in this expression, "stat" refers to the 68.3% confidence interval of the estimated quantity ($X_{\rm cosm}$ in Equation (1) with $X = A_{BB}$) given our observation with non-zero lensing signal ($X_{\rm meas} = 0.69$), and "multi" refers to multiplicative calibration uncertainties. The likelihood of the *B*-mode amplitude is shown in

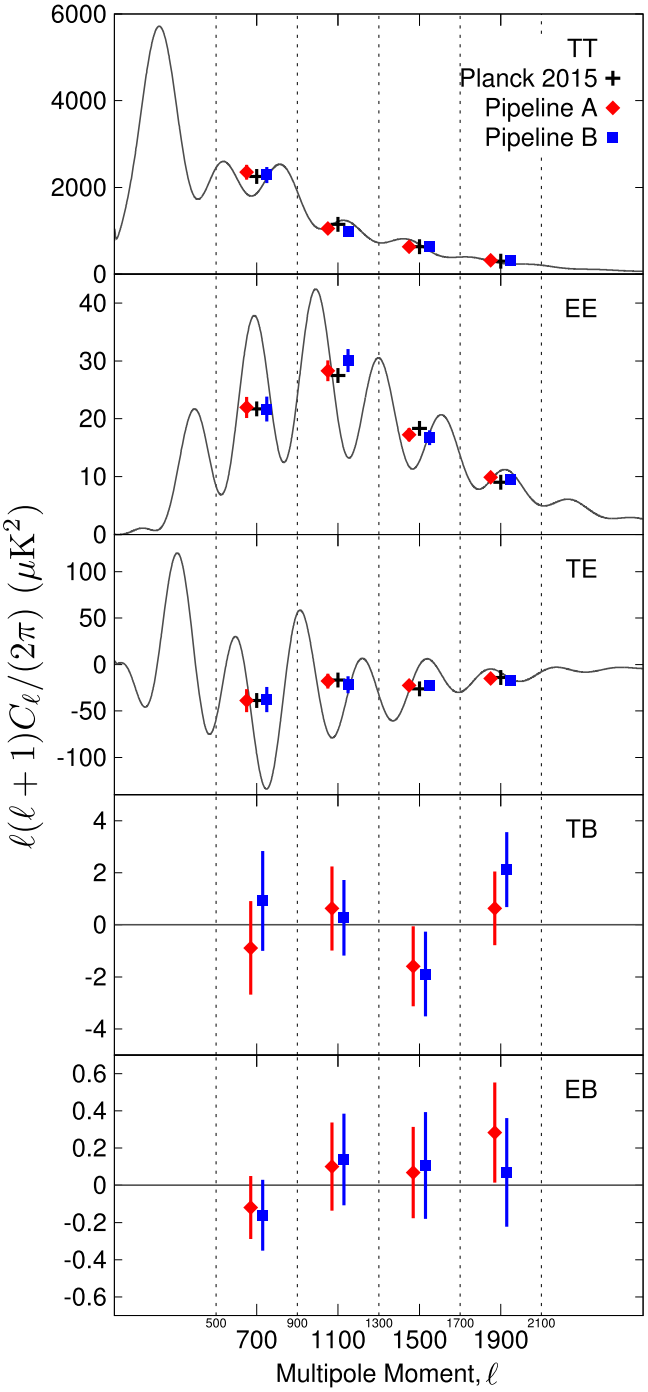

Figure 8. POLARBEAR power spectra from the two-season data sets used for calibration and cross-checks. Red diamonds (blue squares) show the measured band powers from pipeline A (pipeline B). The uncertainty shown for the band powers is the diagonal of the band-power covariance matrix, including beam covariances, and all results take into account the absolute gain factor and global instrument polarization angle (see Section 6). The black curve is a theoretical *Planck* 2015 ΛCDM spectrum, and the black plus signs are the expected binned band powers.

Figure 10. The shift in the estimated amplitude with respect to the null result is due to different field and band-power weighting, which uses the covariance matrix with the *Planck* 2015 ΛCDM model, or $A_{BB} = 1$.

Finally, we fit for the amplitude parameter A_{BB} after subtracting the foreground terms from Section 5, which we denote finally as A_L. We find $A_L = 0.60^{+0.26}_{-0.24}(\mathrm{stat})^{+0.00}_{-0.04}(\mathrm{inst}) \pm 0.14(\mathrm{foreground}) \pm 0.04(\mathrm{multi})$, where "foreground" refers to the total foreground uncertainty. This amplitude can be interpreted as the measured amplitude of the lensing *B*-modes. Table 5 summarizes all of the systematic uncertainties in the measurement of A_L. Although the mean value shifts from the previous measurement in PB14, the change in the mean value is consistent with statistical fluctuation even accounting for the fact that the data have overlap between this result and PB14. Compared to PB14, the uncertainty on the lensing amplitude has been reduced by a factor of two, thanks to the realistic uncertainty estimate as well as the overall larger data set and improved calibration.

8. Conclusions

We measured the CMB *B*-mode angular power spectrum, C_ℓ^{BB}, over the multipole range $500 < \ell < 2100$ from a blind analysis of data from the first two seasons of POLARBEAR observations. We doubled the sensitivity on the lensing amplitude compared to the first-season result (PB14) and rejected the null hypothesis of no *B*-mode polarization with 3.1σ confidence. After subtracting the new estimated foreground contamination based on the *Planck* 2015 data, which were unavailable in PB14, we found the amplitude of the lensing signal to be $A_L = 0.60^{+0.26}_{-0.24}(\mathrm{stat})^{+0.00}_{-0.04}(\mathrm{inst}) \pm 0.14(\mathrm{foreground}) \pm 0.04(\mathrm{multi})$.

The data were analyzed by two independent pipelines, giving results in agreement. These results are supported by an extensive suite of null tests in which 12 divisions of data were used to finalize the data selection and by an estimate of systematic errors from nine sources of instrumental contamination using a detailed instrument model. We found that all of the systematic uncertainties are small compared to the statistical uncertainty in the measurement. To motivate a comprehensive evaluation of the data set and prevent observer bias in data selection and analysis, the selection criteria and systematic errors were determined before the *B*-mode power spectra themselves were examined by the two independent analysis pipelines. In Figure 11, we present our measurement alongside recent measurements by SPTPOL (Keisler et al. 2015), ACTPOL (Louis et al. 2017), and the Keck Array (The BICEP2 and Keck Array Collaborations et al. 2015).

We reported previous evidence for gravitational lensing of the polarized CMB in POLARBEAR data (The POLARBEAR Collaboration et al. 2014b) on the same sky area studied in this work using the PB14 data set. An updated lensing analysis using the first two seasons of POLARBEAR observations described in this paper will be presented soon in a separate publication. After the two seasons reported here, we installed a continuously rotating HWP in 2014 May (Takakura et al. 2017), and we have been observing a larger patch of the sky ($\sim$700 deg^2) since then, targeting inflationary *B* modes at degree angular scales. Results from the analysis of this data set will be reported in future publications.

Foreground contamination is one of the main limiting factors in our measurement of *B* modes. Neither *WMAP* nor *Planck* 2015 has enough sensitivity at small angular scales to sufficiently constrain the polarized synchrotron and dust amplitude in the POLARBEAR observations reported here. Dedicated multifrequency observations are therefore needed to obtain better constraints. New receivers (POLARBEAR-2) at 95, 150, 220, and 270 GHz with the sensitivity to reach inflationary tensor-to-scalar ratio $\sigma(r) < 0.01$ are under development (Inoue et al. 2016) and are being implemented on the Simons Array telescopes (Suzuki et al. 2016). Such improvements will enable the Simons Array to enter

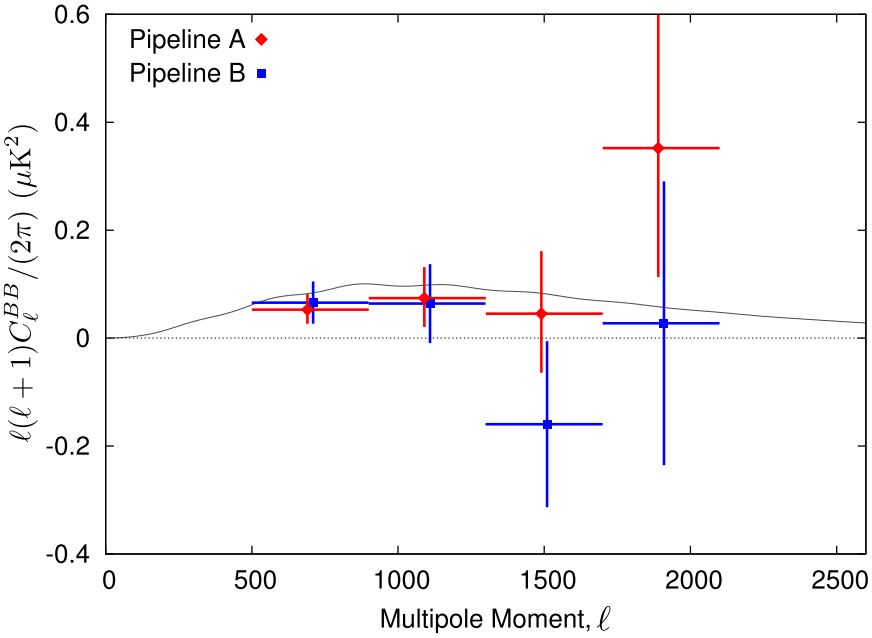

Figure 9. POLARBEAR *B*-mode angular power spectrum from the two-season data sets. Red diamonds (blue squares) show the measured band powers from pipeline A (pipeline B). The plotted error bars correspond to the 68.3% confidence intervals of the statistical uncertainty only. The multiplicative uncertainty (due, e.g., to the absolute calibration uncertainty) and systematic uncertainties are not plotted, but can be found in Table 5. The black curve is a theoretical *Planck* 2015 ΛCDM lensing *B*-mode spectrum shown for comparison.

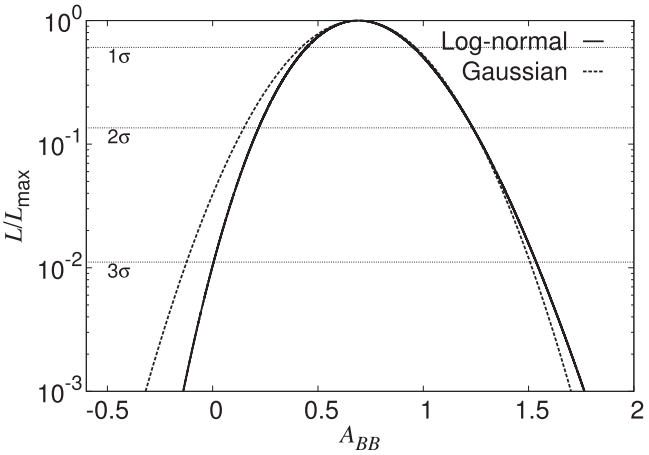

Figure 10. Likelihood curve of the *B*-mode amplitude modeled by an offset log-normal distribution. The curve modeled by the Gaussian distribution is also shown for comparison. The intersections of the curves with the dashed horizontal lines give the bounds with 1σ, 2σ, and 3σ confidence intervals. The log-normal functional form captures the asymmetric shape of the likelihood function due to sample variance.

into an era of precise CMB polarization measurements, improving our understanding of the early and late universe physics.

J.P. acknowledges support from the Science and Technology Facilities Council (grant number ST/L000652/1) and from the European Research Council under the European Union's Seventh Framework Programme (FP/2007-2013)/ERC Grant Agreement No. [616170]. The POLARBEAR project is funded by the National Science Foundation under grants No. AST-0618398 and No. AST-1212230. The James Ax Observatory operates in the Parque Astronómico Atacama in northern Chile under the auspices of the Comisión Nacional de Investigación Científica y Tecnológica de Chile (CONICYT). This research used resources of the Central Computing System, owned and operated by the Computing Research Center at KEK, the HPCI system (Project ID:hp150132), and the National Energy Research Scientific Computing Center, a DOE Office of Science User Facility supported by the Office of Science of the U.S. Department of Energy under contract No. DE-AC02-05CH11231. In Japan, this work was supported by MEXT KAKENHI grant Nos. JP15H05891 and 21111002, and JSPS KAKENHI grant Nos. JP26220709, JP24111715, and JP26800125. This work was supported by World Premier International Research Center Initiative (WPI), MEXT, Japan. This work was supported by JSPS Core-to-Core Program. In Italy, this work was supported by the RADIOFORE-GROUNDS grant of the European Union's Horizon 2020 research and innovation programme (COMPET-05-2015, grant agreement number 687312) as well as by the INDARK INFN Initiative. The McGill authors acknowledge funding from the Natural Sciences and Engineering Research Council of Canada and the Canadian Institute for Advanced Research. J.P. acknowledges support from the Science and Technology Facilities Council (grant number ST/L000652/1) and from the European Research Council under the European Union's Seventh Framework Programme (FP/2007-2013)/ERC Grant Agreement No. [616170]. G.F. acknowledges support from the CNES postdoctoral program. D.B. acknowledges support from NSF grant AST-1501422. D.B. acknowledges support from FONDECYT postdoctoral grant number 3150504. C.F. acknowledges support from grants HST-AR-13886.001-A, IGPP LANL 368641, NASA NNX16AF39G, and the Ax Foundation for Cosmology at UC Irvine. C.R. acknowledges support from an Australian Research Council's Future Fellowship (FT150100074). M.A. acknowledges support from CONICYT UC Berkeley-Chile Seed Grant (CLAS fund) Number 77047, Fondecyt Project 1130777, the DFI Postgraduate Scholarship Program, and the DFI Postgraduate Competitive Fund for Support in the Attendance to Scientific Events. R.D. acknowledges support from CONICYT grants FONDECYT

Table 5
Summary of the Reported POLARBEAR Systematic Uncertainties

Type	Source of Systematics	Effect on D_ℓ^{BB} [10^{-4} μK^2]	Effect on A_{BB}
Instrument (Section 4.4)	Gain drift	8.5	0.009
	Differential gain	9.3	0.010
	Differential beam size	0.4	0.000
	Differential beam ellipticity	0.1	0.000
	Differential and boresight pointing	5.7	0.008
	Instrument and relative polarization angle	6.7	0.008
	Electrical crosstalk	2.5	0.003
	Total	33.3	0.037
Astrophysical foreground	Galactic dust (Section 5.1)	63.5 ± 123.3	0.071 ± 0.138
	Galactic synchrotron (Section 5.1)	1.4 ± 2.1	0.002 ± 0.002
	Radio and dusty galaxies (Section 5.2)	13.4 ± 5.5	0.019 ± 0.005
	Subtotal	78.3 ± 123.4	0.092 ± 0.138
Analysis[a]	Ground pickup removal	0.5 ± 1.7	0.001 ± 0.002
	E-to-*B* leakage due to filter subtraction	2.5	0.003
	Subtotal	2.9 ± 1.7	0.003 ± 0.002
	Total	81.2 ± 123.4	0.095 ± 0.138
Multiplicative effect	Absolute gain uncertainty (Section 6)		±3.0%
	Beam uncertainty (Section 6)		±1.0%
	Polarization efficiency (Section 3.4)		±3.3%
	Transfer function[a]		±3.9%
	Total		±6.0%

Note. Note that the third column represents the effect on D_ℓ^{BB} at the first ℓ = [500, 900] bin; on the other hand, the fourth column represents the total effect on A_L in the multipole range $500 \leqslant \ell \leqslant 2100$.
[a] The residual of the ground pickup removal and *E*-to-*B* leakage subtraction, and the sensitivity of the transfer function to different cosmologies are evaluated using the same methodology of PB14. The systematic bias and uncertainty from "Analysis" is subtracted from the measured band powers and propagated in pipeline A.

1141113, QUIMAL 160009, and Anillo ACT-1417. S.T. was supported by a Grant-in-Aid for JSPS Research Fellow.

Appendix
Detector Gains: Modeling Saturn's Rings

For the PB14 data release, we used only observations of Saturn taken between 2012 June and September (four months of data), and we assumed the temperature of Saturn to be constant, with $T_{\rm sat}$ = 148 K_{RJ}. However, the analysis of Saturn observations over a longer period (2012 May–2014 April) exhibited variations of up to 10% over time (Peloton 2015). We investigated several possible explanations, such as a misestimation of the apparent diameter of the planet, dependency in the elevation, miscorrection of the atmosphere contribution, stability of the stimulator, change in the main beam parameters, or even changes in the sidelobes over time, but none gave an explanation for the shift of approximately 10% in between the two seasons. This shift was, however, explained by taking into account the influence of Saturn's rings on the planet flux. Even if we cannot resolve the rings,[44] their inclination with respect to the plane of observation from the Earth produces a variation over time in the measured microwave brightness temperature, as described and shown in, e.g., Dunn et al. (2002), Weiland et al. (2011), and Hasselfield et al. (2013). The contribution of the rings to the total temperature brightness of Saturn is twofold: they obscure and therefore reduce the flux from the main disk, but they also radiate at a lower temperature and contribute to the total signal through a mix of scattering and thermal re-emission of planetary radiation (at 150 GHz, the thermal emission dominates over the scattering). The change in opening angle (i.e., the angle made by the plane of the rings and the line of sight of the observer) allows us to break the degeneracy between the contribution of the disk and that of the rings. We follow the two-parameter empirical model proposed by *WMAP* (Weiland et al. 2011) by modeling the total brightness temperature of Saturn as a contribution from the disk $T_{\rm disk}$ with seven extended surrounding rings described by one global effective temperature $T_{\rm ring}$.[45] The individual contributions from those two parameters to the total brightness is given by the orientation of the system at the moment of the observation.

We use 132 observations of Saturn between 2012 May and 2014 April, selected for their high quality of data and spanning ring-opening angles from $\sim$12° to $\sim$23°. The observations are combined into periods of 15–30 days, taking the uncertainty in each combined measurement to be the error in the mean of the contributing data. The model fit parameters and uncertainties ($\chi^2 \sim 2$ per degree of freedom) are $T_{\rm disk}$ = 126.8 ± 2.7 K_{RJ} and $T_{\rm ring}$ = 16.3 ± 6.0 K_{RJ} (after applying the absolute calibration derived from the CMB temperature spectrum as described in Section 6). The uncertainties include a statistical contribution and a systematic contribution from the wafer-to-wafer variations. The

[44] Given the angular size of Saturn with respect to our beam size, we cannot resolve the details of the planet. The variations in the atmosphere of Saturn (pole/equator differences, clouds, seasonal variations, etc.) are also not taken into account here.

[45] $T_{\rm disk}$ and $T_{\rm ring}$ temperatures are assumed to be time invariant.

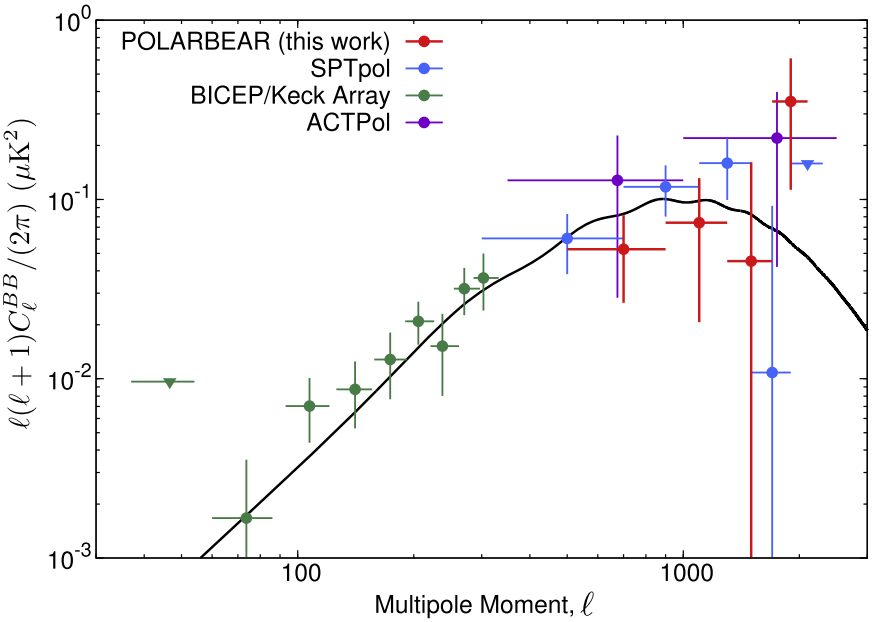

Figure 11. *B*-mode polarization power spectrum measurements from POLARBEAR (this work by pipeline A), SPTPOL (Keisler et al. 2015), ACTPOL (Louis et al. 2017), and the Keck Array (The BICEP2 and Keck Array Collaborations et al. 2015). Uncertainties correspond to a 68.3% confidence level, while upper limits are quoted at a 95.4% confidence level. The black curve is a theoretical *Planck* 2015 ΛCDM spectrum.

ACT collaboration provides complementary measurements at 148 GHz for ring-opening angles from $-2°$ to $12°$ in Hasselfield et al. (2013). They found $T_{\rm disk} = 133.8 \pm 3.2$ K$_{\rm RJ}$ and $T_{\rm ring} = 17.7 \pm 2.2$ K$_{\rm RJ}$, which are consistent with our values. On the other hand, the *Planck* 2015 collaboration recently reported a measurement of Saturn's disk temperature rescaled at 147 GHz (Planck Collaboration et al. 2016e). They found a temperature of the main disk $T_{\rm disk} = 145.7 \pm 1.1$ K$_{\rm RJ}$ higher than the POLARBEAR and ACT values. However, Figure 10 in Planck Collaboration et al. (2016e) seems to suggest that the ring temperatures between *Planck* 2015 and ACT, and therefore POLARBEAR, are in agreement.

ORCID iDs

P. A. R. Ade https://orcid.org/0000-0002-5127-0401
K. Arnold https://orcid.org/0000-0002-3407-5305
F. Bianchini https://orcid.org/0000-0003-4847-3483
Y. Chinone https://orcid.org/0000-0002-3266-857X
G. Fabbian https://orcid.org/0000-0002-3255-4695
A. H. Jaffe https://orcid.org/0000-0003-2086-1759
C. L. Reichardt https://orcid.org/0000-0003-2226-9169
N. Whitehorn https://orcid.org/0000-0002-3157-0407

References

Arnold, K., Ade, P. A. R., Anthony, A. E., et al. 2012, Proc. SPIE, 8452, 84521D
Aumont, J., Conversi, L., Thum, C., et al. 2010, A&A, 514, A70
Bennett, C. L., Larson, D., Weiland, J. L., et al. 2013, ApJS, 208, 20
Bonavera, L., González-Nuevo, J., Argüeso, F., & Toffolatti, L. 2017, MNRAS, 469, 2401
Bond, J. R., Jaffe, A. H., & Knox, L. 2000, ApJ, 533, 19
De Zotti, G., Ricci, R., Mesa, D., et al. 2005, A&A, 431, 893
Dunn, D. E., Molnar, L. A., & Fix, J. D. 2002, Icar, 160, 132
Ferté, A., Grain, J., Tristram, M., & Stompor, R. 2013, PhRvD, 88, 023524
Fuskeland, U., Wehus, I. K., Eriksen, H. K., & Næss, S. K. 2014, ApJ, 790, 104
George, E. M., Reichardt, C. L., Aird, K. A., et al. 2015, ApJ, 799, 177
Górski, K. M., Hivon, E., Banday, A. J., et al. 2005, ApJ, 622, 759
Grain, J., Tristram, M., & Stompor, R. 2009, PhRvD, 79, 123515
Grain, J., Tristram, M., & Stompor, R. 2012, PhRvD, 86, 076005
Hasselfield, M., Moodley, K., Bond, J. R., et al. 2013, ApJS, 209, 17
Hivon, E., Górski, K. M., Netterfield, C. B., et al. 2002, ApJ, 567, 2
Inoue, Y., Ade, P., Akiba, Y., et al. 2016, Proc. SPIE, 9914, 99141I
Keating, B. G., Shimon, M., & Yadav, A. P. S. 2013, ApJL, 762, L23
Keisler, R., Hoover, S., Harrington, N., et al. 2015, ApJ, 807, 151
Kermish, Z. D., Ade, P., Anthony, A., et al. 2012, Proc. SPIE, 84521C
Krachmalnicoff, N., Baccigalupi, C., Aumont, J., Bersanelli, M., & Mennella, A. 2016, A&A, 588, A65
Louis, T., Grace, E., Hasselfield, M., et al. 2017, JCAP, 06, 031
Matsuda, F. 2017, Thesis, Univ. of California, San Diego, https://search.proquest.com/docview/1916808409
Murphy, T., Sadler, E. M., Ekers, R. D., et al. 2010, MNRAS, 402, 2403
Peloton, J. 2015, Theses, Univ. Paris Diderot-Paris VII, https://tel.archives-ouvertes.fr/tel-01257383
Planck Collaboration, Adam, R., Ade, P. A. R., et al. 2016a, A&A, 594, A1
Planck Collaboration, Adam, R., Ade, P. A. R., et al. 2016b, A&A, 594, A10
Planck Collaboration, Adam, R., Ade, P. A. R., et al. 2016c, A&A, 594, A9
Planck Collaboration, Ade, P. A. R., Aghanim, N., et al. 2014, A&A, 571, A1
Planck Collaboration, Ade, P. A. R., Aghanim, N., et al. 2016d, A&A, 594, A20
Planck Collaboration, Akrami, Y., Ashdown, M., et al. 2016e, arXiv:1612.07151
Planck Collaboration Int. XXII 2015, A&A, 576, A107
Planck Collaboration Int. XXX 2016, A&A, 586, A133
Poletti, D., Fabbian, G., Le Jeune, M., et al. 2016, A&A, 600, A60
QUIET Collaboration, Araujo, D., Bischoff, C., et al. 2012, ApJ, 760, 145
Smith, K. M. 2006, PhRvD, 74, 083002
Suzuki, A., Ade, P., Akiba, Y., et al. 2016, JLTP, 184, 805
Takakura, S., Aguilar, M., Akiba, Y., et al. 2017, JCAP, 05, 008
The BICEP2 Collaboration, Ade, P. A. R., Aikin, R. W., Barkats, D., et al. 2014, PhRvL, 112, 241101
The BICEP2 and Keck Array Collaborations, Ade, P. A. R., Ahmed, Z., Aikin, R. W., et al. 2015, ApJ, 811, 126
The BICEP2 and Keck Array Collaborations, Ade, P. A. R., Ahmed, Z., Aikin, R. W., et al. 2016, PhRvL, 116, 031302
The BICEP2/Keck and Planck Collaborations, Ade, P. A. R., Aghanim, N., Ahmed, Z., et al. 2015, PhRvL, 114, 101301
The POLARBEAR Collaboration, Ade, P. A. R., Akiba, Y., Anthony, A. E., et al. 2014a, ApJ, 794, 171
The POLARBEAR Collaboration, Ade, P. A. R., Akiba, Y., Anthony, A. E., et al. 2014b, PhRvL, 113, 021301
Weiland, J., Odegard, N., Hill, R., et al. 2011, ApJS, 192, 19
Wrobel, J. M., Patnaik, A. R., Browne, I. W. A., & Wilkinson, P. N. 1998, BAAS, 30, 1308